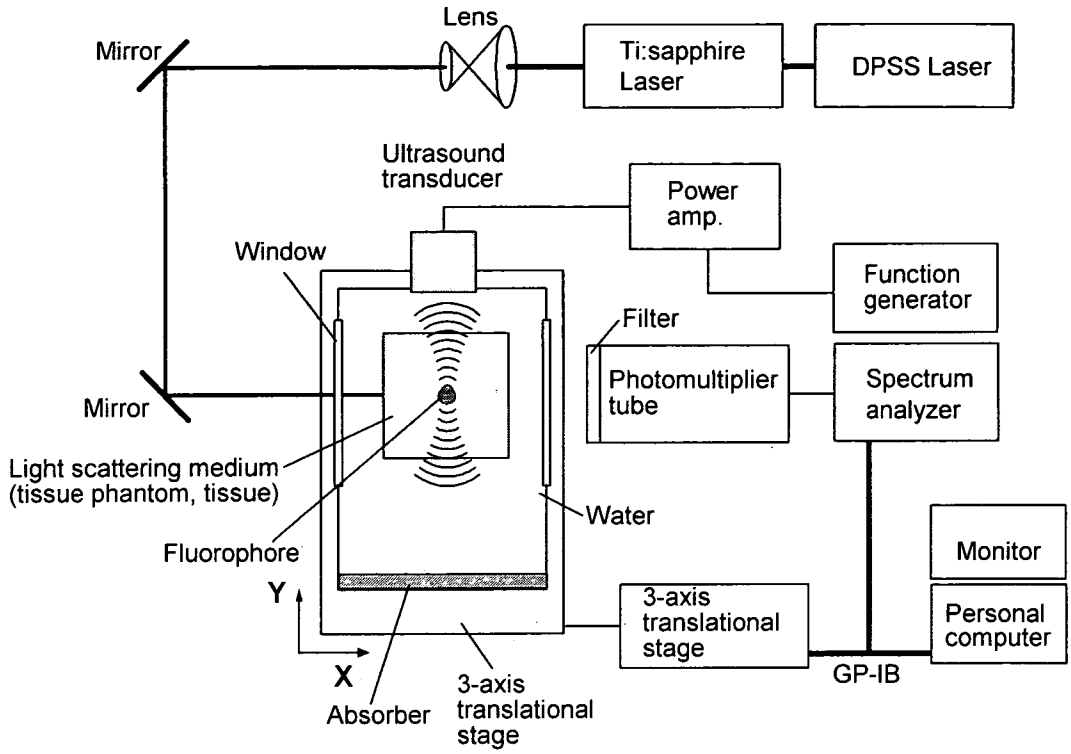

Fig. 1. Schematic of the experimental setup. A water tank equipped with an ultrasound transducer is set on the X-Y-Z auto-stage; a tissue phantom is fixed in place without touching the water tank.

3. RESULTS AND DISCUSSION

3.1 Tomographic images obtained with a tissue phantom which has a fluorofore in the centre of the scattering media

A tomographic image of fluorescence observed with a phantom of light-scattering gel that contains a single fluorescent region in the center is shown in Fig. 2 (a). The area of higher signal intensity on the image corresponds to the site of fluorophore embedded in the phantom. The profile of the signal intensity along the X-axis on the image sectioned at the center of the phantom including the fluorescent region is indicated in Fig. 2 (b). The full-width at half-maximum of the profile is *ca.* 3 mm, corresponding to the diameter of the embedded fluorescent region. Considering the 3-mm beam diameter of a focused ultrasound field, the spatial resolution observed in the image is appropriate. A photograph of the phantom is depicted in Fig. 2 (c). It shows the top view of the phantom, indicating the size of the phantom measuring 40 × 40 mm. Scanned area in the phantom is 20 × 20 mm of centre region. Taking into consideration the reduced scattering coefficient of the phantom, which is estimated as 0.85 mm^{-1} at the measured wavelength, this technique is potentially applicable for biological tissues. It suggests the availability for the measurement of the deep site of actual living bodies with using near-infrared light.

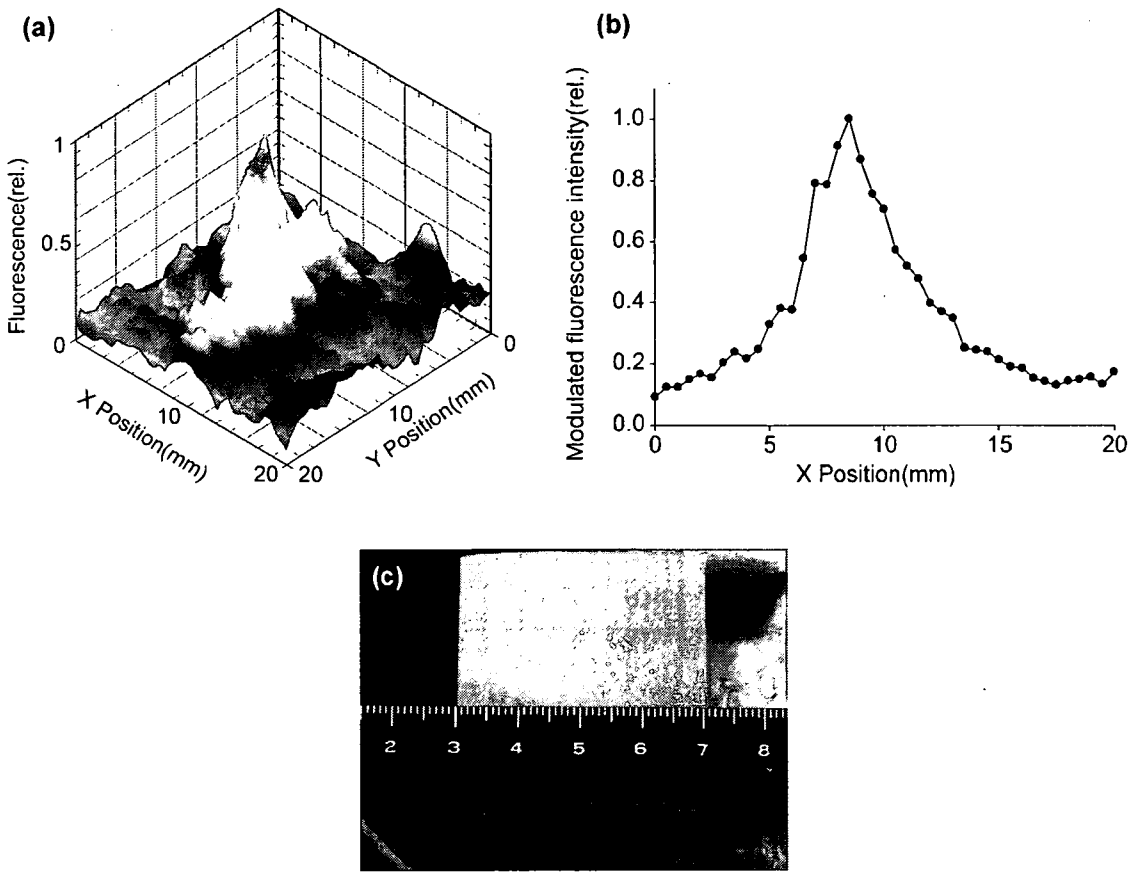

Fig. 2 (a) A tomographic image of fluorescence observed with a tissue phantom of light-scattering gel with a single fluorescent region in the phantom's center. (b) A profile of the signal intensity along with X-axis on the image sectioned at the center of the phantom, which contains the embedded fluorescent region. (c) A top view of a tissue phantom with a scale showing the dimension. Embedded region of fluorophore is in the centre of the phantom.

3.2 Tomographic image obtained with using a porcine muscle which has a fluorophore in the centre

A tomographic image of fluorescence observed with a porcine muscle that contains a localized fluorescent region in the center is shown in Fig. 3 (a). A localized area of fluorophore at the center of the tissue is detected. The area of higher signal intensity corresponds to the region of fluorophore embedded in the sample. The profile of the signal intensity along the X-axis on the image sectioned at the center of the phantom including the fluorescent region is indicated in Fig. 3 (b). The peak width of the profile is *ca.* 3 mm in the full-width at half-maximum. It matches the diameter of the embedded fluorescent region and the size of ultrasound focus. A photograph of tissue sample inserted in a holder is shown in Fig. 3(c). With consideration of the signal-to-noise ratio obtained in this experiment and scattering coefficient of the living tissue, this result suggests the potential of this technique for imaging of fluorescence buried in biological tissues with *ca.* 30mm depth. Considering this, further progress in the development of scanning techniques, for example using an arrayed ultrasound transducer, can provide a method for measuring fluorescence in bodies for clinical use. This technique is expected to facilitate the expansion of fluorescent probes' use for biological applications throughout the fields of life science and clinical medicine.

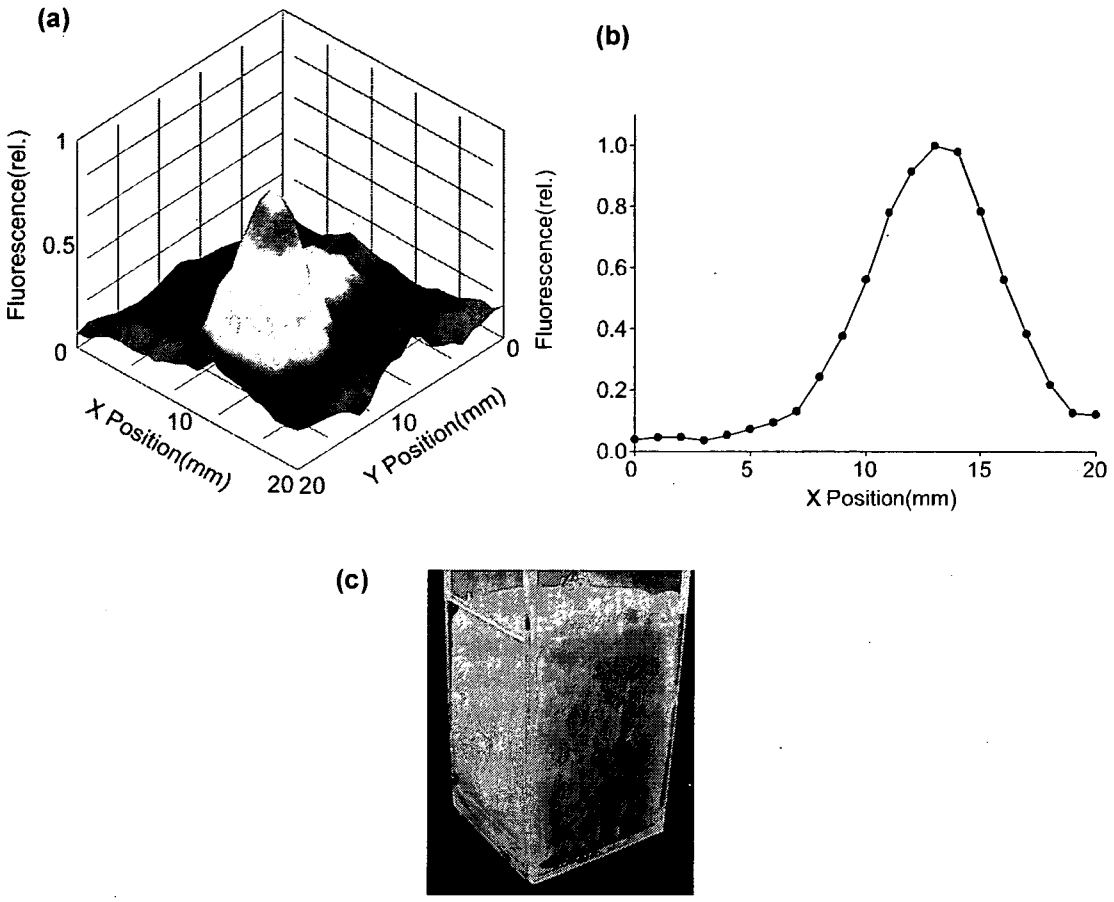

Fig. 3. (a) A tomographic image of fluorescence observed with a porcine muscle with a single fluorescent region in the phantom's center. (b) A profile of the signal intensity along with X-axis on the image sectioned at the center of the tissue, which contains the embedded fluorescent region. (c) An aspect of a tissue sample with a holder.

REFERENCES

1. T. Vo-Dinh ed., *Biomedical Photonics Handbook*, CRC Press, Boca Raton, (2003).
2. L. V. Wang, S. L. Jacques, and X. Zhao, "Continuous-wave ultrasonic modulation of scattered laser light to image objects in turbid media," *Opt. Lett.* 20, 629 (1995).
3. M. Kobayashi, T. Kasamatsu, Y. Shibuya, M. Enomoto, "Optical visualization of ultrasound pressure fields in turbid media based on a coherent detection imaging technique," *Jpn. J. Appl. Phys.* 45, 1836 (2006).
4. M. Kobayashi, T. Mizumoto, Y. Shibuya, M. Enomoto, M. Takeda, "Fluorescence tomography in turbid media based on acousto-optic modulation imaging", *Appl. Phys. Lett.* 89, 181102 (2006).

Journal of Experimental Botany, Vol. 58, No. 3, pp. 465–472, 2007
doi:10.1093/jxb/erl215 Advance Access publication 8 December, 2006
This paper is available online free of all access charges (see http://jxb.oxfordjournals.org/open_access.html for further details)

Journal of Experimental Botany

RESEARCH PAPER

Highly sensitive determination of transient generation of biophotons during hypersensitive response to cucumber mosaic virus in cowpea

Masaki Kobayashi[1,*], Kensuke Sasaki[1], Masaru Enomoto[1] and Yoshio Ehara[2,†]

[1] *Tohoku Institute of Technology, 35-1, Yagiyama Kasumicho, Taihaku-ku, Sendai, 982-8577 Japan*

[2] *School of Food, Agricultural and Environmental Sciences, Miyagi University, 2-2-1, Hatatate, Taihaku-ku, Sendai, 982-0215 Japan*

Received 16 March 2006; Revised 26 September 2006; Accepted 27 September 2006

Abstract

The hypersensitive response (HR) is one mechanism of the resistance of plants to pathogen infection. It involves the generation of reactive oxygen species (ROS) which have crucial roles in signal transduction or as toxic agents leading to cell death. Often, ROS generation is accompanied by an ultraweak photon emission resulting from radical reactions that are initiated by ROS through the oxidation of living materials such as lipids, proteins, and DNA. This photon emission, referred to as 'biophotons', is extremely weak, but, based on the technique of photon counting imaging, a system has been developed to analyse the spatiotemporal properties of photon emission. Using this system, the dynamics of photon emission which might be associated with the oxidative burst, which promotes the HR, have been determined. Here, the transient generation of biophotons is demonstrated during the HR process in cowpea elicited by cucumber mosaic virus. The distinctive dynamics in spatiotemporal properties of biophoton emission during the HR expression on macroscopic and microscopic levels are also described. This study reveals the involvement of ROS generation in biophoton emission in the process of HR through the determination of the inhibitory effect of an antioxidant (Tiron) on biophoton emission.

Key words: Biophoton, cucumber mosaic virus, hypersensitive response, imaging, reactive oxygen species, ultraweak photon emission, visualization.

Introduction

Recently, 'biophotons' from plants have attracted attention for providing novel information for visualizing the physiological states of plants (Kobayashi *et al.*, 1997; Havaux, 2003; Bennett *et al.*, 2005; Mansfield, 2005). Imaging using biophotons offers a novel methodology for assessing plant physiology. Biophotons are spontaneous ultraweak photon emissions that originate from biochemical metabolic reactions of living organisms. Biophotons do not require external chemiluminescent or bioluminescent reagents, nor do they require transgenic techniques for labelling. In mammals too, biophoton emissions are known to occur during the immunological response; they originate from oxidative bursts in immunocytes. Similarly, the generation of biophotons in plant responses involved in resistance to infection has been revealed.

Biophoton emission, sometimes referred to as ultraweak photon emission or ultraweak/dark bioluminescence, is commonly recognized as radiation with wavelengths from visible to near-infrared induced through electronically excited molecules that exist in living cells. Emissions result from reactions involving radicals accompanying the production of reactive oxygen species (ROS). The emission intensity is $<10^{-15}$ W cm^{-2}, which is a level 10^{-3}–10^{-6} times lower than the visible level. Although the intensity is extremely low, photons possess information related to metabolic production of ROS associated with various types of physiological and/or pathological states in living systems. This is generally observed and

* To whom correspondence should be addressed. E-mail: masaki@tohtech.ac.jp
† Professor Yoshio Ehara passed away on 21 April 2006. The authors mourn his passing.
Abbreviations: CMV, cucumber mosaic virus; HR, hypersensitive response; PCD, programmed cell death; ROI, region of interest; ROS, reactive oxygen species.

applicable for plants, animals, and microbes (Inaba, 1988; Devaraj *et al.*, 1997; Kobayashi, 2003*a*, *b*). Various studies have analysed plant physiological responses to various stresses, including both biotic (Roschger, 1991; Makino *et al.*, 1996; Kobayashi *et al.*, 2003; Bennett *et al.*, 2005; Mansfield, 2005) and abiotic stress (Kobayashi *et al.*, 1996, 1997; Ohya *et al.*, 2000; Havaux, 2003). A highly sensitive system has been developed for *in situ* imaging of biophoton emissions to visualize ROS-related physiological changes in plants, and the first image is shown of biophoton emission resulting from the hypersensitive response (HR) in the cowpea (*Vigna unguiculata*)–cucumber mosaic virus (CMV) system (Kobayashi *et al.*, 2003).

The HR process is identified as a gene-for-gene theory describing the interaction of a translation product of an avirulence gene (*Avr* gene) of a pathogen with a ligand by a receptor encoded by a corresponding resistance gene (*R* gene) of a host, described as incompatible plant–pathogen interactions (Baker *et al.*, 1997). In the case of the cowpea–CMV system, the *Avr* gene is known to be RNA2, which codes for the 2a protein, a subunit of viral replicase components. In addition, the *R* gene is identified with the *Cry* locus, inherited as a single dominant trait (Nasu *et al.*, 1996; Karasawa *et al.*, 1997, 1999). The HR results in localized cell death at the initial infection site to delimit the spread of the invading pathogen. Confinement of the virus is exhibited as the formation of local lesions with cell death within 24 h after inoculation. During the HR, ROS production, termed the oxidative burst, is known to contribute through its important role in the diverse array of defence mechanisms. As an intracellular signal for triggering the defence response and extracellular direct agents for defence, ROS mediate the expression of defence-related genes, alteration of the membrane potential, and cell wall modification through oxidative cross-linking of cell wall structural proteins and through the production of antimicrobial compounds: phytoalexins, polyphenols, and chitinase (Mehdy, 1994; Baker *et al.*, 1997; Vranova *et al.*, 2002). In the case of the HR in the cowpea–CMV system, ROS are thought to contribute to signal transduction, and might act as a toxic agent leading to host cell death through lipid peroxidation (Roschger, 1991). In contrast, Bennett *et al.* (2005) reported biophoton generation in the HR of *Arabidopsis thaliana* and claimed that the increases of cytosolic calcium and nitric oxide were key roles for biophoton emission, but ROS elevation was not necessary.

In this study, the transient generation of biophotons is characterized using a highly sensitive imaging technique based on a photon counting imaging system. The spatiotemporal dynamics of biophoton emissions on macroscopic and microscopic levels and the spectral distribution of biophoton emission with evaluation of ROS involvement in biophoton emissions are also described.

Materials and methods

Two-dimensional photon counting imaging and procedures for spatiotemporal analyses of biophoton emission

The imaging system comprises a two-dimensional photon counting tube that is characterized by its large active area, a highly efficient lens system installed in the sample chamber, and electronic equipment for identifying two-dimensional spatial and temporal photoelectron data (Kobayashi *et al.*, 1996, 1999*a*, *b*). The photon counting tube (Model IPD 440; Photek, Ltd, UK) comprises a 40 mm diameter photocathode, a microchannel plate, and a resistive anode for single-photon counting imaging. The detector is incorporated into a specially designed vacuum chamber to cool the device at −35 °C for reduction of dark current and to ensure long-term stability of the device for ultimate sensitivity. This system detects wavelengths of 350–900 nm with a quantum efficiency of 15% at 500 nm, 10% at 600 nm, and 2.4% at 800 nm. The photocathode's active area for imaging is set as 25×25 mm^2. The spatial resolution of the detector, which is determined by the readout precision of the resistive anode incorporated into the photon counting tube, is ~200 μm.

Three types of specially designed lens systems (Fuji Optical Co. Ltd, Tokyo, Japan) are used for adapting three ranges of magnification of 0.33, 1.0, and 5.0. Their respective object sizes are 75×75, 25×25, and 5×5 mm. For improvement of light collection efficiency, their numerical apertures are designed, respectively, at 0.17, 0.5, and 0.65, and the lenses are reduced to six when considering transmittance. The lens system has a built-in shutter mechanism.

Output pulses from the resistive anode in the detector are fed to a position computer (IPD controller; Photek Ltd, UK) to determine the X–Y position of each photoelectron event. The data of the time interval between two successive photoelectron pulses with two-dimensional position data of each photoelectron event are transferred consecutively to a specially designed pulse interval counter that can store 27 bits of timing data simultaneously. The time resolution of data acquisition is determined by a pulse-to-pulse resolution of 10 μs. After data acquisition, data are transferred to a personal computer to reconstruct photon counting images and to analyse spatiotemporal properties. This process produces the intensity kinetics in the regions of interest (ROIs) or the time–space correlation of photoelectrons. The advantage of this system is its capability to set the arbitrary selection of spatial and temporal dimensions of the ROI after measurement. Details of the data collection circuit and data processing for spatiotemporal characterization analyses are presented elsewhere (Kobayashi *et al.*, 1996).

General preparation of plants and viruses, and measurement procedures

The cowpea cv. Kurodane-Sanjaku was used throughout the experiments. Plants were grown and assayed for CMV infection under conditions described elsewhere (Nasu *et al.*, 1996). The yellow strain of CMV, CMV-Y, and the legume strain of CMV, CMV-L, were maintained in tobacco plants and purified as described (Nasu *et al.*, 1996). Extracted primary 10–14-d-old leaves were used for assay by rubbing them with CMV inoculation of 50 μg ml^{-1} of virions in potassium phosphate buffer after dusting with carborundum (#600). Preparation after leaf excision was performed under a weak red light to minimize the effects of fluorescence from leaves by excitation with a room light. Inoculated leaves were put onto a Petri dish with a damp filter paper, and then covered. The dish was mounted on a temperature- (27 °C) controlled dish holder in a light-tight sample chamber of the imaging system. Measurement was carried out continuously for 24 h after inoculation. With respect to data analysis, the first 5 h of data were omitted to eliminate the photon emission originating from delayed fluorescence.

The cell-permeable ROS scavenger Tiron (4,5-dehydroxy-1,3-benzene-disulphonic acid, disodium salt; Sigma-Aldrich Corp.) was used to examine the effect of antioxidants. Two plants were excised at the epigeal stem 24 h prior to inoculation: one was soaked in 100 μM Tiron solution; the other was soaked in water as a control. After leaf excision, viral inoculation was performed similarly on each leaf half. Both leaves were placed onto the same Petri dish for biophoton measurement.

Spectral analyses of biophoton emissions

Spectral analyses of ultraweak photon emissions were carried out using a filter-type spectrometer: a photon counter equipped with coloured glass filters with spectral resolution of 20–50 nm. Details of the system and the process for construction of the spectrum were described in a previous report (Kobayashi *et al.*, 2001).

Results

Biophoton emission images of leaves during HR and their spatiotemporal properties

Temporal changes of biophoton emissions obtained under various treatment conditions are shown in Fig. 1. A time

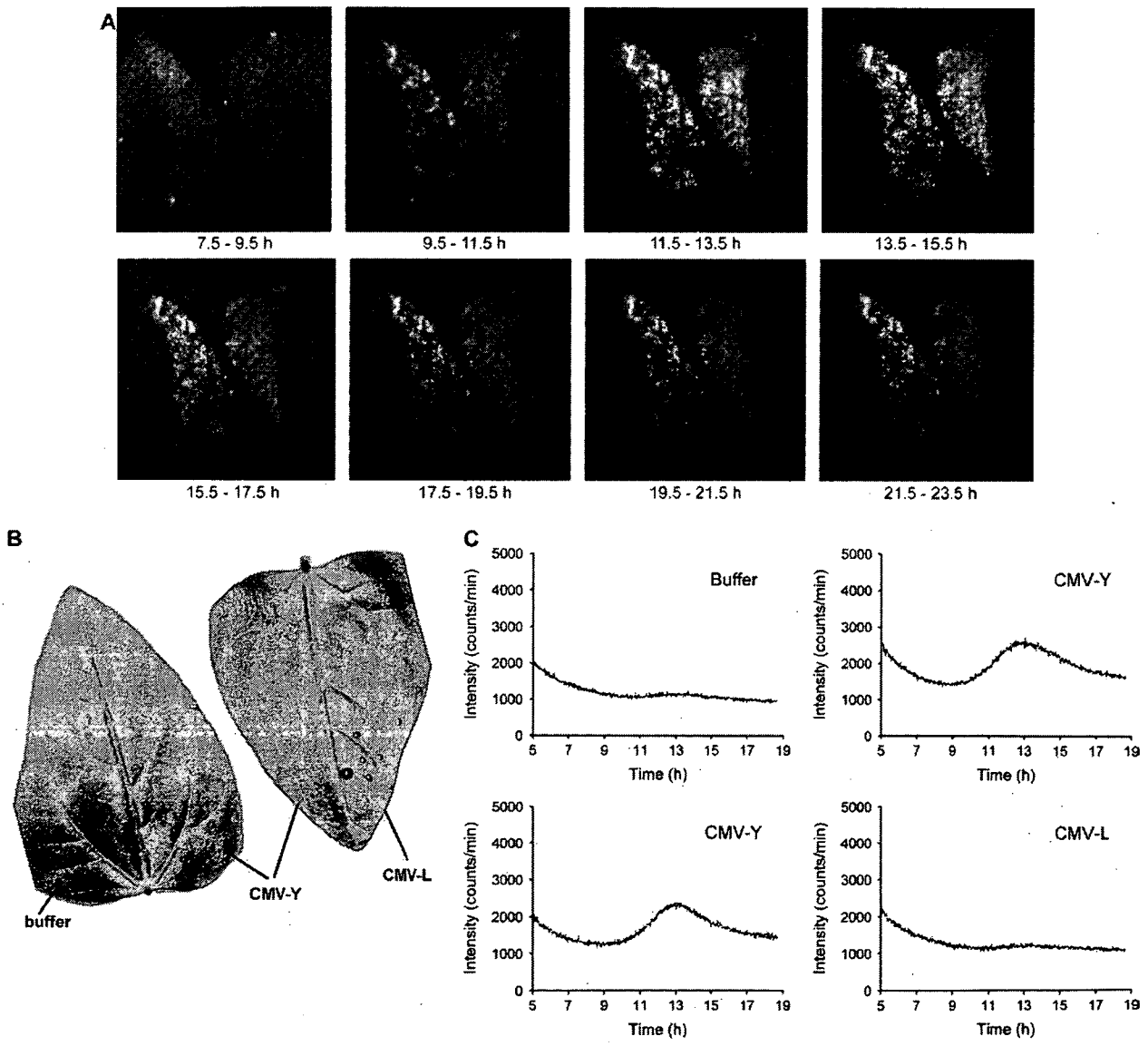

Fig. 1. Biophoton emission imaging of the hypersensitive response observed on cowpea leaves after inoculation with cucumber mosaic virus and its comparison among different strains of virus, CMV-Y, CMV-L, and buffer treatment. (A) Time sequence of biophoton emission images of two leaves after inoculation observed using the ×0.33 lens system. Images are constructed with time integration over the time range indicated below each image. (B) A sample photograph taken 24 h after inoculation. The condition of inoculation treatment is indicated. (C) Comparison of time-courses of ultraweak photon emission among different treatment regions for CMV-Y, CMV-L, and buffer.

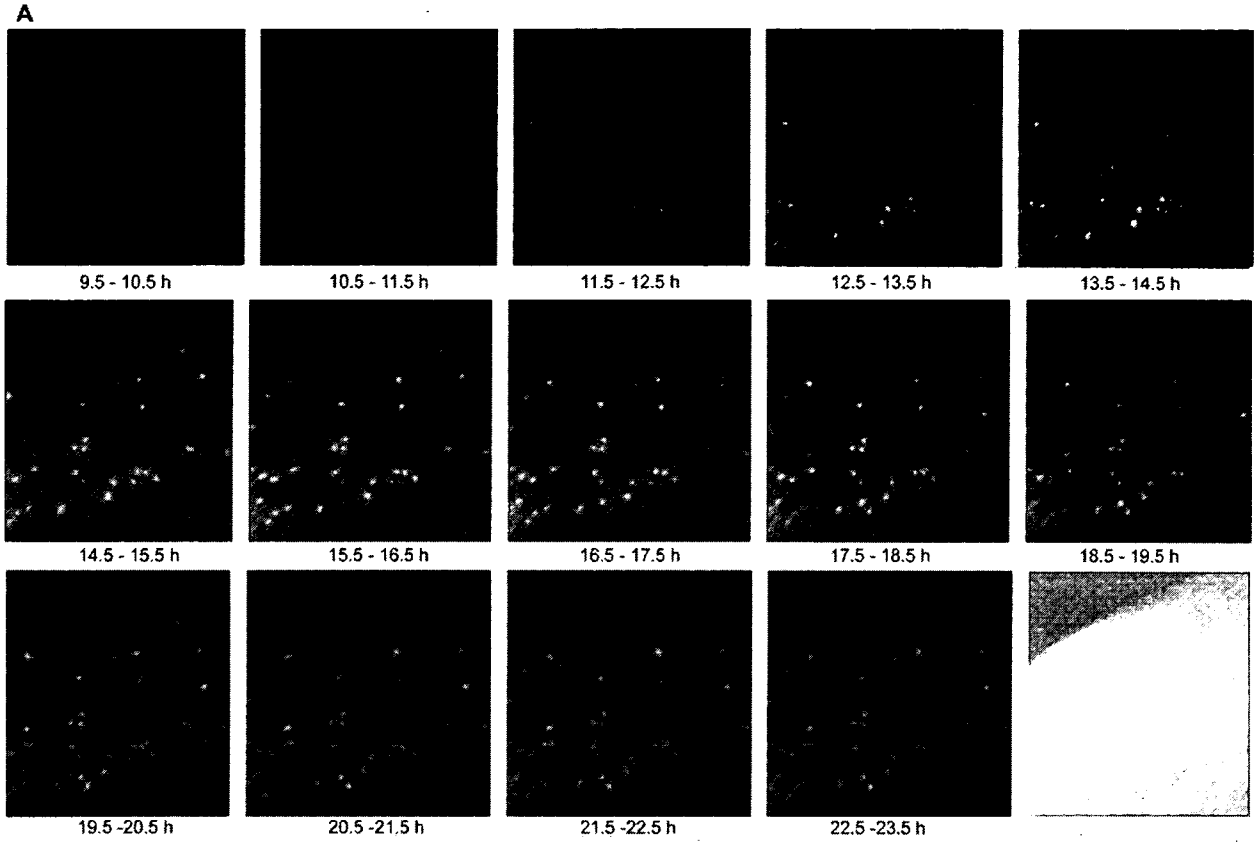
A
9.5 - 10.5 h
10.5 - 11.5 h
11.5 - 12.5 h
12.5 - 13.5 h
13.5 - 14.5 h
14.5 - 15.5 h
15.5 - 16.5 h
16.5 - 17.5 h
17.5 - 18.5 h
18.5 - 19.5 h
19.5 -20.5 h
20.5 -21.5 h
21.5 -22.5 h
22.5 -23.5 h

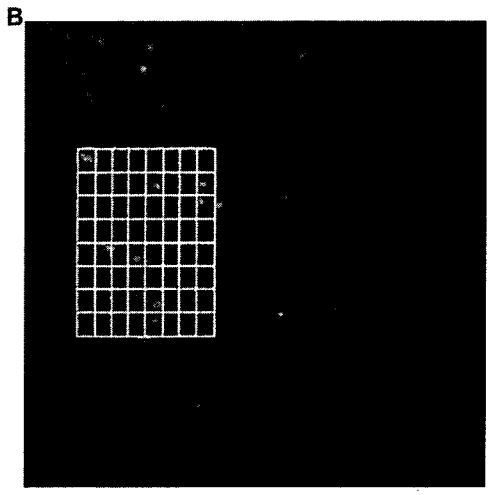
B

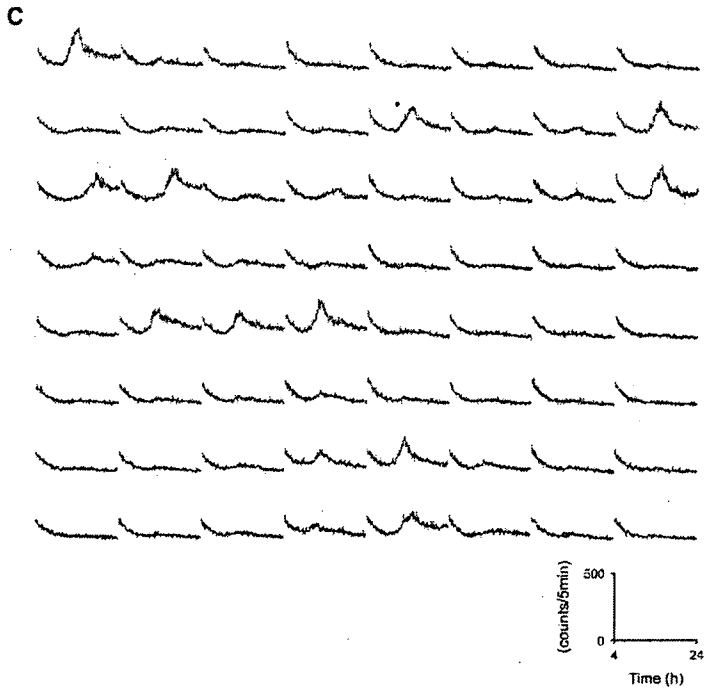
C
500
0
(counts/5min)
4
24
Time (h)

sequence of photon emission images of two leaves after inoculation observed using the ×0.33 lens system are indicated in Fig. 1A. In Fig. 1A, the right half of the left leaf and the left half of the right leaf were inoculated with CMV-Y—the CMV strain eliciting HR. The left half of the left leaf was treated with virus-lacking buffer solution as a control. The right half of the right leaf was treated with CMV-L, which is the strain which does not elicit the HR. The time range indicated below the images in Fig. 1A represents the time elapsed after inoculation. The photograph in Fig. 1B shows the sample configuration. This photograph was taken 24 h after inoculation, indicating the expression of the local lesion on the leaf halves that had been inoculated with CMV-Y. From Fig. 1A, two regions where CMV-Y was inoculated show temporal augmentation of localized ultraweak photon emission as bright spots. In contrast, the area treated with CMV-L and buffer showed no remarkable changes in intensity. Six independent experiments in the same conditions were performed: similar results were obtained in each case. In Fig. 1C, time-courses of total photon emission intensity in each leaf half are shown, indicating that the intensity of CMV-Y-infected regions was enhanced markedly in photon emission from 10 h to 16 h after infection, which preceded the appearance of symptoms. On the buffer-treated region, the intensity showed monotonously decreased photon emission, demonstrating the effect of delayed fluorescence from the leaves. A temporal increase of photon emission was not observed. The CMV-L-treated region also showed no remarkably greater amount of emissions than the area treated with CMV-Y. Biophoton emission images acquired during each 2 h after inoculation (Fig. 1A) also indicate the orchestrated increase of light emission from infected spots, which is maximal at 13.5 h after inoculation. As shown in the photograph taken after the measurement (24 h after the inoculation), localized lesions are recognized as dark spots. These visible lesions appeared only on the CMV-Y-treated regions. Biophoton generation in the early stage of the HR implies a relationship between the photon emission and an initial trigger leading to the HR.

Figure 2 depicts an image obtained using ×1.0 magnification comparable with the object area of 25×25 mm. Temporal changes of photon emission images are shown in Fig. 2A; they are clearly identifiable spots of photon emission. These spots were confirmed as consistent with sites of emerged lesions after the measurement (24 h after the inoculation). The time-courses of the intensity in the ROI, which was sectioned into 8×8 regions demarcated as the white lattice in Fig. 2B, are indicated in Fig. 2C along with 64 graphs of time-courses of intensity on areas placed at corresponding positions for spatiotemporal assay of emissions. The ROIs were chosen to comprise a single spot in each region. The timing of the increase and peak pattern in photon emissions is recognized as roughly parallel among selected spots, and it indicates that the timing of the appearance of the peaks is between 9 h and 19 h after inoculation.

Figure 3 portrays a microscopic biophoton emission image that shows enlarged spots of a single local lesion using a ×5.0 magnification lens system. Figure 3A shows that several spots are contained in the image, with diameters of ~1 mm. An extracted region (Fig. 3B), demarcated with the white box in Fig. 3A, was analysed to show the varied pattern of development of emission peaks in a single spot. The inner region demarcated with the white box in Fig. 3B was sectioned into 8×8 regions and spatiotemporal properties were analysed. Figure 3C shows the result obtained, indicating that although the intensity level is higher at the central region than in the peripheral region, the configuration of temporal changes of emission peaks is similar over the whole selected region within the indicated time resolution of 15 min.

Biophoton emission spectrum during HR

The biophoton emission spectrum during augmentation of photon emission was determined as shown in Fig. 4, representing a distinct peak at 720 nm. This spectrum is the average of those obtained within the time range of peak formation. Emission spectra obtained in the other time region were comparable before and after the emission peak. The emission peak corresponds to spontaneous photon emissions from dark-adapted leaves or isolated chloroplasts, as reported previously (Hideg *et al.*, 1991), implying that the chlorophyll molecules are the source of photon emissions during HR.

Effect of ROS scavenger on biophoton emission

Figure 5 shows the effect of Tiron treatment. Lower induction of transient augmentation of biophoton emission was observed on the Tiron-treated leaf (Fig. 5A, left leaf) than on the control leaf (Fig. 5A, right leaf). Figure 5B shows time-courses of biophoton emission intensity obtained by the sum of counts in each region of inoculation. On the Tiron-treated leaf, transient generation of photon emission was diminished. After measurement,

Fig. 2. Biophoton emission imaging of the hypersensitive response observed on cowpea leaves after inoculation with cucumber mosaic virus (CMV-Y). (A) Time sequence of biophoton emission images from a leaf after inoculation observed using a ×1.0 lens system. Images are constructed with time integration over the time range indicated below each image. (B) Biophoton emission image obtained with integration over the total measurement time. The white lattice indicates the region of interest selected to analyse the spatiotemporal properties of photon emission. (C) Spatiotemporal properties of biophoton emission. Each small graph represents the time-course of photon emission intensity at the located position corresponding to regions designated in (B). The time scale in each figure is 4–24 h after inoculation.

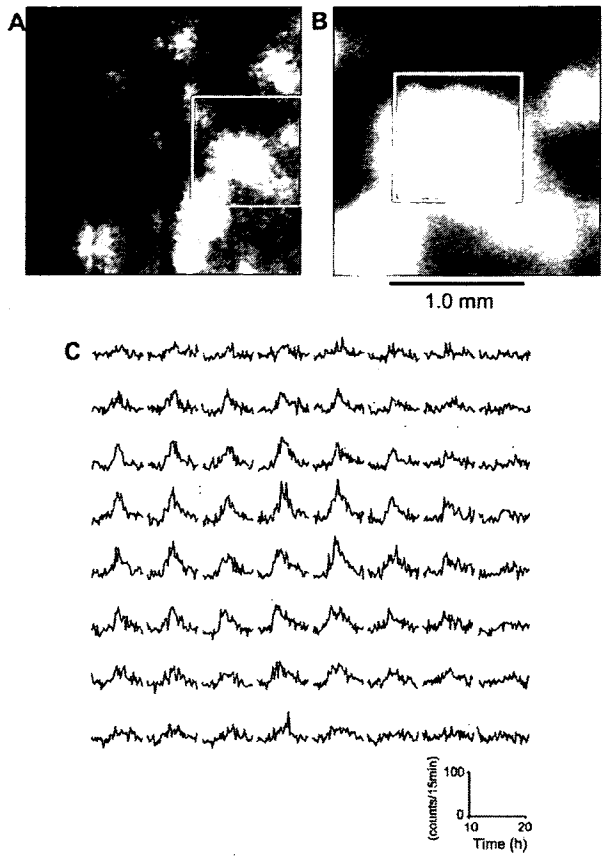

Fig. 3. Biophoton emission imaging of the hypersensitive response observed on cowpea leaves after inoculation with cucumber mosaic virus (CMV-Y). (A) Biophoton emission images observed using the ×5.0 lens system, constructed with time integration over the total measurement time (24 h). (B) An extracted image from (A) to select a single spot. The selected region is demarcated with a white box in (A). (C) Spatiotemporal properties of biophoton emissions from a single spot of the local lesion. The analysed area is demarcated with a white box in (B). The time scale in each figure is 10–20 h after inoculation.

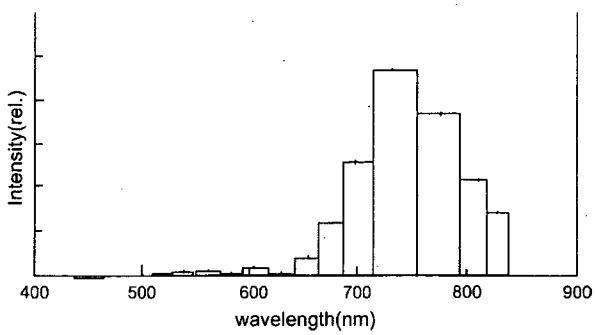

Fig. 4. Spectrum of biophoton emission during the hypersensitive response observed on cowpea leaves after inoculation with the cucumber mosaic virus (CMV-Y). The spectrum was the average of those obtained within the time range of peak formation.

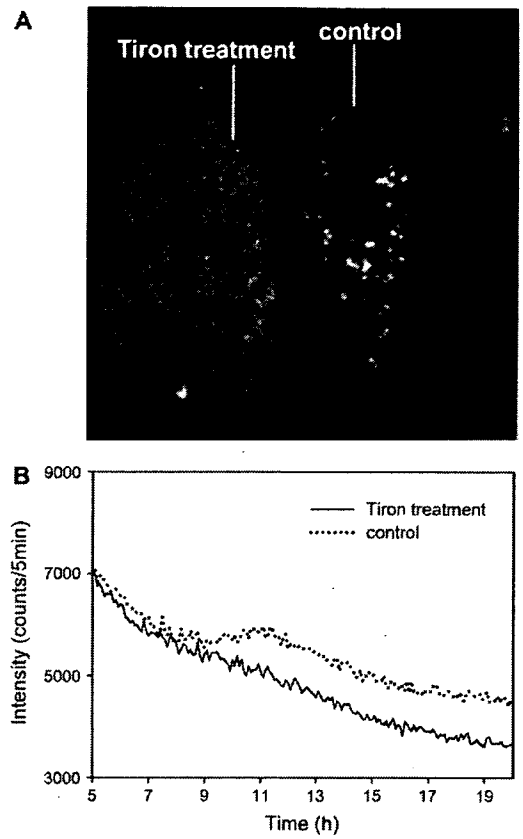

Fig. 5. Effects of ROS scavengers on biophoton emission during the hypersensitive response in the cowpea–CMV system. (A) Comparison of biophoton emission images of a Tiron-treated leaf (left) and a control leaf (right). Inoculation was performed on half of each leaf, as indicated. (B) Comparison of time-courses of biophoton emission intensities on inoculated regions of the two leaves. The straight line shows the time-course of the Tiron-treated leaf. The dotted line shows that of the control.

necrotic lesions were not recognized. Four independent experiments under the same conditions were performed: similar results were obtained in each case. This result suggests that ROS generation involves the HR process and the biophoton generation process.

Discussion

Transient generation of biophotons (as a sort of 'photon burst') at sites corresponding to the local lesion was determined. Two-dimensional images of biophoton emissions and their time sequence during expression of the HR at infected sites depicted the synchronous emergence of photons. The time range of the peak configuration in intensity among individual spots dispersed within 10–16 h after inoculation, suggesting that the increased photon emission is attributed to the oxidative burst. A biphasic oxidative burst, characterized as rapid responses occurring

within the minutes–hours time range (phase I) and later production within hours–days (phase II), is known to appear due to fungal, bacterial, or viral elicitors (Grant and Loake, 2000; Allan *et al.*, 2001). Although two phases of bursts play a pivotal role in induction of defence mechanisms, ROS production kinetics and ROS types and their function are thought to differ. In addition, phase I is suggested as not always correlating with plant disease, but is important as a priming of phase II. In contrast, phase II, which is specific to avirulent pathogens, correlates with plants' resistance or susceptibility to the pathogen. The tobacco–tobacco mosaic virus (TMV) system is also reported to be accompanied by two phases of ROS production. It is suggested that oxidative phase II responses correlate with HR and cell death, in contrast to the phase I response. The latter is necessary for triggering the defence mechanism, but is insufficient for the final resistance response (Allan *et al.*, 2001). The transient augmentation of biophoton emission observed in the present experiments is presumed to originate in ROS generation in phase II, in which ROS are postulated to serve as anti-pathogens and in host cell necrosis (Mehdy, 1994; Rusterucci *et al.*, 1996; Baker *et al.*, 1997; Riedle-Bauer, 2000) with an added role as signal mediators leading to the subsequent defence mechanism. For the cowpea–CMV system, the elicitor *Avr* gene product is known to be the 2a protein, which is a subunit of the viral replicase components of CMV. Consequently, early expression of HR is inferred to result from this gene-for-gene recognition mechanism. The timing of increased biophoton emission after inoculation, which appears from 10 h to 16 h, is inferred to be consistent with the time for replication after virus entry. Suppression of transient augmentation of biophoton emission and emergence of the HR with Tiron treatment (Fig. 5) suggests ROS involvement in biophoton emission and implies a role for ROS in triggering this. This result is inconsistent with the result of Bennett *et al.* (2005). However, it is speculated that the discrepancy arises from the different uptake of ROS scavengers.

Spectral data, shown in Fig. 4, show that the excited species that finally emit photons originate in chlorophyll. It can be assumed that the oxidative damage in chloroplasts is involved in the emission mechanisms. The photon emission mechanism is hypothesized to excite chlorophyll molecules directly by ROS-mediated radical reaction, or indirectly through energy transfer from other excited molecules, such as excited proteins, excited carbonyls, or singlet oxygen through specific amino acid oxidation or lipid peroxidation by ROS (Hideg *et al.*, 1990; Hideg, 1993). Therefore, these excited molecules are also potentially non-chlorophyll emitters. However, chlorophyll is dominant in the case of leaves. The photon emission burst behaviour, which continues for only a few hours, represents the existence of a finely regulated mechanism to result in the HR process and to protect healthy cells from ROS damage. This regulation mechanism may involve the orchestration of cells that form a single visible lesion, as shown in the microscopic measurement in Fig. 3, depicting the parallel increase of photon emissions of both the central and peripheral regions in the spot. Recently, the signalling role of ROS has attracted attention in the context of programmed cell death (PCD) during HR (Levine *et al.*, 1996; Jones, 2001). Cell death induced by HR is also recognized as a part of apoptotic cell death, in common with that found in mammals. Regarding HR, the direct toxic effect of ROS might dominantly lead to necrotic cell death. Alternatively, apoptotic cell death derived by PCD might be essential to the death process (Mittler *et al.*, 1997; Pennell and Lamb, 1997; Mittler, 2002; Vranova *et al.*, 2002). Some studies have concluded that both processes are involved (Breusegem *et al.*, 2001; Houot *et al.*, 2001). It remains unclear whether the observed photon bursts represent the result of a direct attack on the pathogen or the host cell for apoptosis by ROS. The present technique is useful to analyse spatiotemporal dynamics of biophoton emission with high sensitivity. It will serve to elucidate this mechanism further in the near future.

References

Allan AC, Lapidot M, Culver JN, Fluhr R. 2001. An early tobacco mosaic virus-induced oxidative burst in tobacco indicates extracellular perception of the virus coat protein. *Plant Physiology* **126,** 97–108.

Baker B, Zambryski P, Staskawicz B, Dinesh-Kumar SP. 1997. Signaling in plant–microbe interactions. *Science* **276,** 726–733.

Bennett M, Mehta M, Grant M. 2005. Biophoton imaging: a nondestructive method for assaying R gene responses. *Molecular Plant–Microbe Interactions* **18,** 95–102.

Breusegem FV, Vranova E, Dat JF, Inzé D. 2001. The role of active oxygen species in plant signal transduction. *Plant Science* **161,** 405–414.

Devaraj B, Usa M, Inaba H. 1997. Biophotons: ultraweak light emission from living systems. *Current Opinion in Solid State and Material Sciences* **2,** 188–193.

Grant JJ, Loake GJ. 2000. Role of reactive oxygen intermediates and cognate redox signaling in disease resistance. *Plant Physiology* **124,** 21–29.

Havaux M. 2003. Spontaneous and thermoinduced photon emission: new methods to detect and quantify oxidative stress in plants. *Trends in Plant Science* **8,** 409–413.

Hideg E. 1993. On the spontaneous ultraweak light emission of plants. *Journal of Photochemistry and Photobiology B: Biology* **18,** 239–244.

Hideg E, Kobayashi M, Inaba H. 1990. Ultraweak photoemission from dark-adapted leaves and isolated chloroplasts. *FEBS Letters* **275,** 121–124.

Houot V, Etienne P, Petitot AS, Barbier S, Blein JP, Suty L. 2001. Hydrogen peroxide induces programmed cell death features in cultured tobacco BY-2 cells, in a dose-dependent manner. *Journal of Experimental Botany* **52,** 1721–1730.

Inaba H. 1988. Super-high sensitivity systems for detection and spectral analysis of ultraweak photon emission from biological cells and tissues. *Experientia* **44,** 550–559.

Jones AM. 2001. Programmed cell death in development and defense. *Plant Physiology* **125,** 94–97.

Karasawa A, Okada I, Akashi K, Chida Y, Hase S, Nakazawa-Nasu Y, Ito A, Ehara Y. 1999. One amino acid change in cucumber mosaic virus RNA polymerase determines virulent/avirulent phenotypes in cowpea. *Phytopathology* **89,** 1186–1192.

Karasawa A, Ito A, Okada I, Hase S, Ehara Y. 1997. A possible role of RNA 2 of cucumber mosaic virus as a determinant of infection phenotype in cowpea. *Annals of the Phytopathology Society of Japan* **63,** 289–297.

Kobayashi M. 2003*a*. *Spontaneous ultraweak photon emission of living organisms—biophotons—phenomena and detection techniques for extracting biological information. Trends in Photochemistry and Photobiology* **10,** 111–135.

Kobayashi M. 2003*b*. *Modern technology on physical analysis of biophoton emission and its potential for extracting the physiological information.* In: Musumeci F, Brizhik LS, Ho M-W, eds. *Energy and information transfer in biological systems.* Singapore: World Scientific Publications, 157–187.

Kobayashi M, Devaraj B, Usa M, Tanno Y, Takeda M, Inaba H. 1996. Development and applications of new technology for two-dimensional space–time characterization and correlation analysis of ultraweak biophoton information. *Frontiers of Medical and Biological Engineering* **7,** 299–309.

Kobayashi M, Devaraj B, Usa M, Tanno Y, Takeda M, Inaba H. 1997. Two-dimensional imaging of ultraweak photon emission from germinating soybean seedlings with a highly sensitive CCD camera. *Photochemistry and Photobiology* **65,** 535–537.

Kobayashi M, Sasaki S, Suzuki S, Enomoto M, Ehara T. 2003. Detection and analysis of hypersensitive reaction of cowpea (*Vigna unguiculata*) leaf infected with cucumber mosaic virus based on highly sensitive detection of biophoton. *Extended abstracts (The 50th Spring Meeting, 2003); The Japan Society of Applied Physics and Related Societies.* 11390 (in Japanese).

Kobayashi M, Takeda M, Ito KI, Kato H, Inaba H. 1999*a*. *Two-dimensional photon counting imaging and spatiotemporal characterization of ultraweak photon emission from a rat's brain in vivo. Journal of Neuroscience Methods* **93,** 163–168.

Kobayashi M, Takeda M, Sato T, Yamazaki Y, Kaneko K, Ito KI, Kato H, Inaba H. 1999*b*. *In vivo* imaging of spontaneous ultraweak photon emission from a rat's brain correlated with cerebral energy metabolism and oxidative stress. *Neuroscience Research* **34,** 103–113.

Kobayashi M, Usa M, Inaba H. 2001. Highly sensitive detection and spectral analysis of ultraweak photon emission from living samples of human origin for the determination of biomedical information. *Transactions of the Society of Instrument and Control Engineering* **E-1,** 214–220.

Levine A, Pennell RI, Alvarez ME, Palmer R, Lamb C. 1996. Calcium-mediated apoptosis in a plant hypersensitive disease resistance response. *Current Biology* **6,** 427–437.

Makino T, Kato K, Iyozumi H, Honzawa H, Tachiiri Y, Hiramatsu M. 1996. Ultraweak luminescence generated by sweet potato and *Fusarium oxysporum* interaction associated with a defense response. *Photochemistry and Photobiology* **64,** 953–956.

Mansfield JW. 2005. Biophoton distress flares signal the onset of the hypersensitive reaction. *Trends in Plant Science* **10,** 307–309.

Mehdy MC. 1994. Active oxygen species in plant defense against pathogens. *Plant Physiology* **105,** 467–472.

Mittler R. 2002. Oxidative stress, antioxidants and stress tolerance. *Trends in Plant Science* **7,** 405–410.

Mittler R, Simon L, Lam E. 1997. Pathogen-induced programmed cell death in tobacco. *Journal of Cell Science* **110,** 1333–1344.

Nasu Y, Karasawa A, Hase S, Ehara Y. 1996. *Cry,* the resistance locus of cowpea to cucumber mosaic virus strain Y. *Phytopathology* **86,** 946–951.

Ohya T, Kurashige H, Okabe H, Kai S. 2000. Early detection of salt stress damage by biophotons in red bean seedling. *Japanese Journal of Applied Physics* **39,** 3696–3700.

Pennell RI, Lamb C. 1997. Programmed cell death in plants. *The Plant Cell* **9,** 1157–1168.

Riedle-Bauer R. 2000. Role of reactive oxygen species and antioxidant enzymes in systemic virus infections of plants. *Journal of Phytopathology* **148,** 297–302.

Roschger P. 1991. Biophoton response of plants due to environmental stress. In: Inaba H, ed. *The research report on Inaba biophoton project.* Tokyo: Japan Science and Technology Agency, 207–216.

Rusterucci C, Stallaert V, Milat ML, Pugin A, Ricci P, Blein JP. 1996. Relationship between active oxygen species, lipid peroxidation, necrosis, and phytoalexin production induced by elicitins in Nicotiana. *Plant Physiology* **111,** 885–897.

Vranova E, Inzé D, Van Breusegen F. 2002. Signal transduction during oxidative stress. *Journal of Experimental Botany* **53,** 1227–1236.

Breast Cancer
DOI 10.1007/s12282-008-0037-0

CONFERENCE PAPER

Presidential symposium: Individualized diagnosis for tailored treatment of breast cancer

In vivo single molecular imaging and sentinel node navigation by nanotechnology for molecular targeting drug-delivery systems and tailor-made medicine

Motohiro Takeda · Hiroshi Tada · Hideo Higuchi · Yoshio Kobayashi · Masaki Kobayashi · Yuu Sakurai · Takanori Ishida · Noriaki Ohuchi

Abstract The recent advances in nanotechnology have a great potential to improve the prevention, diagnosis, and treatment of human diseases. Nanomaterials for medical applications are expected to grasp pharmacokinetics and the toxicity for application to medical treatment on the aspect of safety of the nanomaterials and nanodevices. We describe a generation of CdSe nanoparticles [quantum dots (QDs)] conjugated with monoclonal anti-HER2 antibody (Trastuzumab), for single molecular in vivo imaging of breast cancer cells. We established a high-resolution in vivo 3D microscopic system for a novel imaging method at the molecular level. The cancer cells expressing HER2 protein were visualized by the nanoparticles in vivo at subcellular resolution, suggesting future utilization of the system in medical applications to improve drug-delivery systems to target the primary and metastatic tumors for made-to-order treatment. We also describe sentinel node navigation using fluorescent nanoparticles for breast cancer surgery in experimental model, which have shown the potential to be an alternative to existing tracers in the detection of the sentinel node if we select the appropriate particle size and wavelength. Future innovation in cancer imaging by nanotechnology and novel measurement technology will provide great improvement, not only in the clinical field but also in basic medical science for the development of medicine.

Keywords Single molecular imaging · Sentinel lymph node biopsy · Nanomedicine · Breast cancer · HER2

This article is based on a presentation delivered at the Presidential Symposium 1, "Breast cancer: individualized diagnosis for tailored treatment," held on 29 June 2007 at the 15th Annual Meeting of the Japanese Breast Cancer Society in Yokohama.

M. Takeda (✉) · H. Tada · Y. Sakurai · T. Ishida · N. Ohuchi
Department of Surgical Oncology, Graduate School of Medicine, Tohoku University 1-1, Seiryo-machi, Aoba-ku, Sendai 980-8574, Japan
e-mail: motot@dl.dion.ne.jp

M. Takeda
Department of Bioengineering and Robotics, Graduate School of Engineering, Tohoku University, Aoba 01, Sendai 980-8579, Japan

H. Higuchi
Biomedical Engineering Research Organization, Tohoku University, Sendai, 6-6-11-901, Aramaki, Aoba-ku, Sendai 980-8579, Japan

Y. Kobayashi
Department of Biomolecular Functional Engineering, College of Engineering, Ibaraki University, 4-12-1 Naka-narusawa-cho, Hitachi, Ibaraki 316-8511, Japan

M. Kobayashi
Division of Electronics, Tohoku Institute of Technology, 35-1 Kasumi-cho, Yagiyama, Taihaku-ku, Sendai 982-8577, Japan

Introduction

Tumor targeting anti-cancer therapeutics by conjugating tumor-specific antibodies is of great interest in oncology, pharmacology, and nanomedicine. This approach will allow to increase therapeutic efficacy and to decrease systemic adverse effect [1, 2]. Quantitative investigation of dynamics of such drug delivery in vivo is crucial to enable the development of more effective drug-delivery systems. One of the best ways to perform this is to apply new technology in biophysics that the positions of proteins are detected quantitatively at the single-molecule level with nanometer precision [3]. However, the specific delivery processes in

vivo is not known at the single-particle level. Conventional imaging modalities such as computed tomography, magnetic resonance imaging, positron emission tomography, and organic fluorescence or luminescence imaging have insufficient resolution to analyze the pharmacokinetics of drugs at the single-particle level in vivo [4].

To address this issue, real-time single-particle tracking using quantum dots (Qdots) has been applied to the study of drug delivery. Qdots, fluorescent nanocrystals, were expected to be a good biomarker because of their intense brightness and stability, in contrast to existing organic dyes and GFP [5, 6]. In cultured cells, single-particle tracking has yielded invaluable information on the function of purified proteins [7, 8]. Recent work shows that the antibody-conjugated Qdots have allowed real-time tracking of single-receptor molecules on the surface of living cells [9]. However, no real-time single-particle tracking in live animals has been reported, and it is uncertain if the single particle of Qdots could be observed or tracked in live animals. We analyzed the movement of single functional Qdots in the tumors of mice from a capillary vessel to cancer cells by a highly sensitive measurement system.

The made-to-order treatment for disease is now strongly expected as well as the evidence-based medicine. In the area of surgery, sentinel node navigation surgery is a major method for performing made-to-order surgery for malignancies. Treatments of cancer with minimum invasive surgery without lymph node dissection based on sentinel lymph node (SN) navigation surgery has become a major concern of made-to-order and low-invasiveness medicine. Some radioisotopes and dyes are utilized for SN detection in the standard method, however, each detection method has advantages and disadvantages. To make up for the disadvantages, we aimed at developing a new noninvasive method using nanosized fluorescent beads of uniform size that could efficiently visualize SN from outside the body and perform experiments to determine the appropriate size and fluorescent wavelength and confirm that uniformly nanosized fluorescent beads have the potential to be an alternative to existing tracers [10, 11] in the detection of the SN in animal. These data should be useful in establishing clinical fluorescence measurement methods in the future.

Materials and methods

Single molecular imaging of breast cancer by quantum dots conjugated with anti-HER2 antibody

We made conjugations of Qdot (Quantum Dot Corporation, Hayward, CA) and trastuzumab (Chugai pharmaceutical Co., LTD, Tokyo, Japan) with a Qdot 800 Antibody Conjugation Kit (Quantum Dot Corporation, Hayward, CA) via poly ethylene glycol (M.W. 2000) and heterobifunctional cross-linker 4-(maleimidomethyl)-1-cyclohexanecarboxylic acid N-hydroxysuccinimide ester (SMCC).

The final concentration of Qdots and trastuzumab complexes (QT complexes) was determined by measuring the conjugate absorbance at 550 nm and using an extinction coefficient of 1,700,000 M^{-1} cm^{-1} at 550 nm.

The human breast cancer cell line KPL-4 [12], which overexpresses HER2 and is sensitive to trastuzumab, was kindly supplied from Dr. J. Kurebayashi (Kawasaki Medical School, Kurashiki, Japan). KPL-4 cells were cultured in Dulbecco's modified Eagle's medium supplemented with 5% fetal bovine serum. A suspension of KPL-4 was transplanted subcutaneously to the dorsal skin of female Balb/c nu/nu mice at 6–10 weeks of age (Charles River Japan, Yokohama, Japan). Mice bearing a tumor volume of 100–200 mm^3 were selected for experiments. All operations on animals were in accordance with the institutional animal use and care regulations. This study was approved by Animal Care and Use Committee of Tohoku University.

QT complexes were injected into tail vein of mice. The mice were placed under anesthesia by the intraperitoneal injection of a ketamine and xylazine mixture at a dosage of 95 and 5 mg/kg, respectively. The temperature of mice was maintained at 37°C by a thermo-plate and objective lens heater. The modified DSFC method [13] was used to fix the exposed mouse tumor on the stage of the microscope. Two sterilized polyvinyl chloride plates (0.5 mm thickness) containing a window were mounted so as to fix the extended double layer of dorsal skin including the tumor site. Skin between chambers sutured with 6-0 nylon around the window, and the tumor could be located in the center of the window and fixed without influence from the beating of the heart and breathing. The tumor was placed surface down on the neutral saline mounted cover slip on a viewing platform of an inverted microscope. The mouse was fixed to a metal plate on the stage designed to stabilize the chamber. Tumors can be visualized directly by means of this setup.

The mice were killed by CO_2 overdose, after imaging. The tumors were removed and divided for histological and immunohistochemical examination. In the histological Qdot uptake study, tumors were frozen and cryosectioned 6 μm thickness, fixed with acetone at 0°C and examined with an imaging system. For immunohistological examination, tumors were fixed in 10% neutral-buffered formalin overnight and then transferred into ethanol before processing and paraffin embedding. Immunohistochemical analysis was performed on paraffin sections at 6-μm

thickness using the HercepTest (Dako Cytomation, CA) to confirm HER2 expression.

As shown in Fig. 1, the optics system for 3D observation consisted primarily of an epi-fluorescent microscope (IX71, Olympus) with modifications, a Nipkow lens type confocal unit (CSU10, Yokogawa) and an electron multiplier type CCD camera (iXon 887, Andor). The confocal unit adopts multi-beam scanning using about a thousand beams that are simultaneously emitted through a pin-hole disk to facilitate high-speed scanning. The EMCCD has advantage that offering unsurpassed sensitivity performance, and has been shown to yield markedly improved SN ratio. The objective lens was moved by a piezo actuator with a feedback loop for stabilizing the position of the focus. A computer controlled the piezo actuator in synchronization with the image acquisitions in order that the objective lens remained within the exposure time of the CCD camera. An area of 30×30 μm^2 was irradiated by a green laser (532 nm, Crystalaser).

The *xy*-position of the fluorescent spot was calculated by fitting to a 2D Gaussian curve. The single molecule could be identified by the fluorescence spot, and quantitative and qualitative information such as velocity, directionality, and transport mode was obtained using time-resolved trajectories of particles. The resolution of the position was determined from the position of immobile QT complexes in a chemically fixed tumor cell. The resolution of the *x* and *y* directions of images taken at an exposure time of 33 ms was 30 nm, taking into consideration the standard deviation.

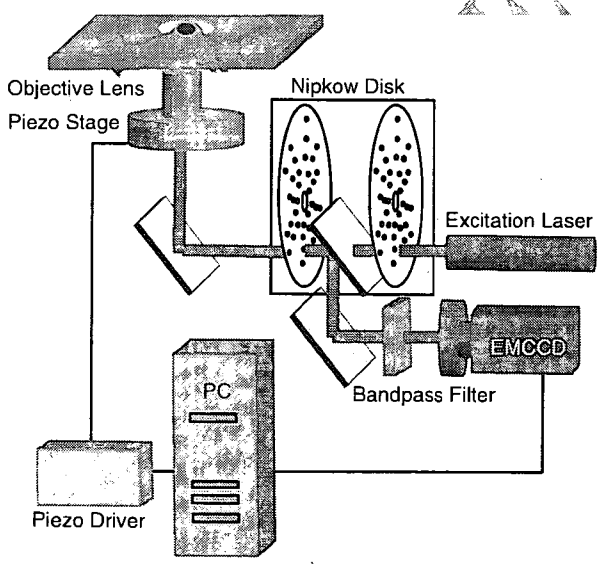

Fig. 1 The 3D intravital imaging system for visualization of QT complexes in a mouse

Sentinel node navigation by nanosized fluorescent beads

We employed "FluoSpheres®" manufactured from high-quality polystyrene microspheres (Molecular Probe Inc, OR, USA) for sentinel node detection. We selected beads of sizes 20, 40, 100, and 200 nm, and fluorescent colors of yellow–green (YG) (excitation/emission maxima at 505/515 nm), dark red (DR) (660/680 nm), far red (FR) (690/720 nm) and infrared (IR) (715/755 nm). The size of beads is very homogeneous, 0.02 ± 0.004 μm in 20-nm size and 0.1 ± 0.005 μm in 100 nm. We designed a laser scanning fluorescence detection system that consists of three lasers, a resonant scanner (resonant frequency/200 Hz), a rotational pulse-stage and a CCD camera (Fig. 2). We used a diode pumped solid-state blue laser (473 nm, 7 mW) as the excitation source of YG fluorescent beads. For excitation of DR, FR, and IR fluorescent beads, we used a He-Ne laser (632.8 nm, 14.6 mW) or a laser diode (657 nm, 3.56 mW). The inguinal and femoral areas were continuously irradiated and scanned over an area of 30x50 mm. The fluorescence image was observed using a CCD camera (XC-EI50, Sony) with an optimum band-pass filter for each fluorescent bead.

In addition, the spectrum of scanned area was analyzed with a spectrometer. Under ether anesthesia, the hair of rats' lower body was removed to avoid autofluorescence of it. Then 50 μl of FluoSpheres® 2% w/v suspension was subcutaneously injected at the footpad of the hind leg. Spectral analysis of fluorescence from rats injected with beads was performed to clarify the signal-to-noise ratio of fluorescence from beads and autofluorescence. After observation from outside the body (through the skin) for 30–180 min, we peeled back the skin at the subcutaneous layer and ascertained the area of lymph nodes with navigation of their specific fluorescence. Then, the lymph nodes were removed and fixed with formalin for histological observation to confirm that the tissue was a lymph node.

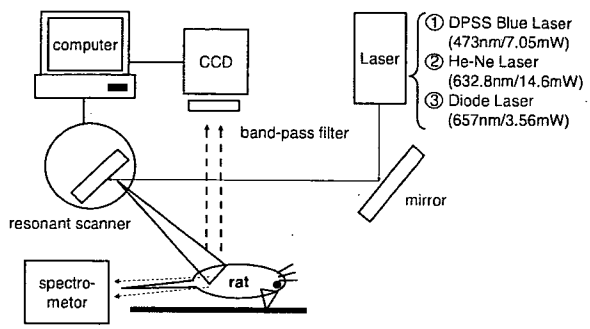

Fig. 2 Fluorescence imaging system for sentinel node detection using nanosized particles

Results

Single molecular imaging of breast cancer by semiconductor quantum dots conjugated with anti-HER2 antibody

The molar ratio of trastuzumab to the Qdots of the QT complexes was approximately 3:1. KPL-4 cell membrane and QT complexes strongly bound 5 min after mixture of KPL-4 and 10-nM QT complexes. Six hours after the mixing, the signals from the QT complexes were found mainly in the cytosol neighboring the nucleus, suggesting that the QT complexes were endocytosed. Qdots without trastuzumab did not bind or accumulate in the KPL-4 cells. A control study using AH109A cells, a HER2 negative cell line, also showed no binding of the QT complexes, indicating that QT complexes selectively bind to the HER2 protein.

A tumor-bearing mice model was prepared with subcutaneous implantation of KPL-4. A single Qdot in the tumor-bearing mice was observed using a high-resolution intravital imaging system through the DSFC. This system captures images of single Qdots at a video rate of 33 ms per frame. The DSFC was firmly mounted on the microscope stage to minimize the distorting influence of the heartbeat and breathing. 3D confocal intravital images of single QT complexes were taken by moving an objective lens. 3D images of the tumor were taken by reconstructing 10–20 confocal images from the surface of the mice to a depth of 150 mm inside the tumor through the DSFC. Fluorescence micro-angiography was performed after injection of the QT complexes into the tail vein. The membranes of the KPL-4 tumor cells were clearly stained with QT complexes at 6 h after the injection. Up to 24 h after the injection, the QT complexes had been internalized into and increased in the tumor cells.

After in vivo tumor imaging of the mice, histological examination of the chemically fixed tumors was performed to confirm that QT complexes in the living mice exhibit activity on the KPL-4 cells. QT complexes observed under the 3D microscope were located at the cell membrane and near the nuclear membrane. The position of the objective was fixed and 300–3,000 sequential confocal 2D images (total 10–100 s) were taken at this fixed position. Within 30 s after the injection, the current of the QT complex in a vessel was observed. When we could observe a vessel and cells clearly, the single QT complex in the current of the tumor vessel was then analyzed. The fluorescence image of the circulating QT complexes was not a circle but an ellipse and sometimes a line at the video rate because QT complexes at times moved >1 mm in a single frame. The speed of the movement of the single particles was calculated from the positional changes of the centroid of the QT complex images. The average speed of each complex ranged from 100 to 600 μm/s, in agreement with a previous report by another method [14]. Each particle exhibited slow and fast movement in the bloodstream. Such fast and slow movement characteristics could be induced by the pulse and nonuniform current within a vessel such as the Hagen–Poiseuille current. The slow speed of the complexes inside a tumor vessel would be important to locate pores between the vessel cells and then moved out through these pores.

Focusing on the vessel walls, a movement was observed of the QT complex extravasated from the intravascular space. The edge of the vascular inner surface was not clear on a single-frame image. Therefore, all the images obtained were averaged to precisely determine the position of the edge. The complexes were positioned first on the vascular surface and then extravasated. This is the first example of video rate observation of extravasation of nanoparticles, such as Qdots, in a mouse model.

Two hours after the injection, many complexes had migrated into the tumor interstitial area close to the tumor vessels. Most of the movement of the complexes was random in both orientation and speed, indicating that complexes diffuse by the Brownian motion exerted by thermal energy. The average diffusion coefficient of the complexes was 0.0014 mm^2/s, much smaller than that at free diffusion in solution ($\sim$10 mm^2/s). Many complexes also moved randomly within a restricted small area of $\sim$1 mm in diameter and then hopped by $\sim$1 mm. The movement was restricted by a cage formed by the extracellular matrix.

Six hours after the injection, QT complexes had bound to the KPL-4 cell membrane on which the HER2 protein is located. We successfully captured specific images of the QT complexes bound to the cell membrane. Movements of a single QT complex are identified in single frames. To identify the positions of the tumor vessels and cells in living mice without further fluorescence staining, images were averaged. Many QT complexes bound to the cell membrane exhibited Brownian motion within a restricted region of $\sim$500 nm in diameter. This region is significantly larger than the area of $\sim$30 nm, which was drawn by position noise of the complexes fixed on a coverslip, indicating the movement is due to the anchor of the HER2 to a flexible component of the cytoskeleton such as an actin filament [15]. The QT complexes restricted to the small area initiated linear movement in one direction along the cell membrane with speed of 400–600 nm/s and traveled for several micrometers.

We also observed in pursuing the transport of QT complexes from the peripheral region of the cell to the perinuclear region. The QT complex in a given cell moved almost straight towards the cell membrane with a velocity of 100–300 nm/s, changed direction to parallel to the cell

membrane, and moved toward the cell nucleus at a velocity of ~600 nm/s. Finally, the directional movement of the QT complex ceased and Brownian motion commenced within a small area, ~1 μm in a diameter, near the nucleus. The first two movements, straight towards and along the cell membrane, would most likely be produced by the transport of an acto-myosin system binding to vesicle containing QT complexes [16], because the actin filaments in cultured cells are highly concentrated in the peripheral region of cells. Movement towards the nucleus would most likely be on a microtubule transported by dynein [17] since there are almost no actin filaments near the nucleus, but rather, a high concentration of microtubules.

Sentinel node navigation by nanosized fluorescent beads

We performed the experiment on four types of beads with diameters of 20, 40, 100, and 200 nm. In the experiment using 20-nm beads, 22 ft from 13 rats were tested. SNs were detected in 10 ft of 22 (45%) by fluorescence contrast as shown in Fig. 3. The time of detection from injection was 0–6 min. The average time for detection was 2.5 min and the median time was 2 min. With the 40-nm beads, SNs were detected in 50 of 72 ft (69%). The time of detection from injection was 0 to 28 min. SNs in 42 ft were detected within 5 min. They were the most representative cases (84%). The average time was 4.6 min and the median time was 3 min. With 100-nm beads, SNs were detected in two of 10 ft (20%). The average and median times were both 56 min. With the 200-nm beads, SNs were detected in seven of 18 ft (39%). The average time was 127 min. The median time was 135 min. In the 40- and 20-nm experiments, there was a significant difference in both the positive rate and average time. In the same way, we compared 40 with 100- or 200-nm beads.

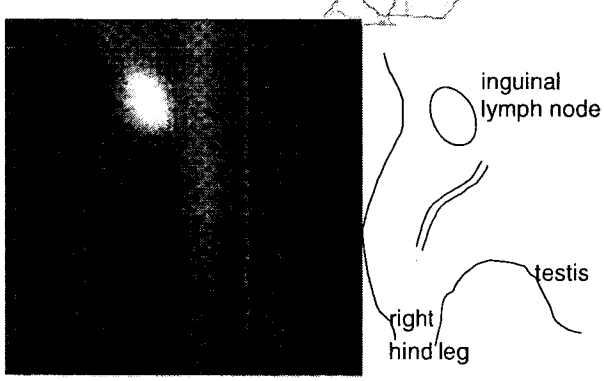

Fig. 3 Fluorescence image of right inguinal node and its illustration for sentinel node imaging using nanosized fluorescent particle in rat

We investigated three excitation and emission wavelengths with the 40-nm beads, yellow–green (YG), dark red (DR) and infrared (IR). Beads of 40 nm in diameter were found to be the most suitable size in the previous experiment. In the experiment using YG, 10 ft from five rats were tested. SNs in three of 10 ft (30%) were observed by fluorescence measurement. With DR, SNs in 24 of 31 ft (77%) were observed and with IR, SNs in 23 of 31 ft (74%) were observed. DR and IR have advantage of positive rate of fluorescence detection as compared with YG.

In these experiments, four different fluorescent wavelengths 515, 680, 720, and 755 nm were studied. DR and IR were more sensitive than YG in the detection rate experiments with 40 nm. There was no significant difference in detection rate, but in average time between DR and IR. However, spectral analysis of DR and IR showed that IR has a higher signal-to-noise ratio compared to DR.

Discussion

In the study for single molecular imaging of cancer, we captured the specific delivery of single QT complexes in tumor vessels to the perinuclear region of tumor cells in live mice after QT complexes had been injected into the tail vein of mice. Six stages were detected (Fig. 4), (1) vessel circulation, (2) extravasation, (3) movement into the extracellular region, (4) binding to HER2 on the cell membrane, (5) movement from the cell membrane to the perinuclear region after endocytosis and (6) in the perinuclear region. The transport speed of QT complexes in each process was highly variable, even in the vessel circulation. The movement of the complexes in each process was also found to be "stop-and-go", i.e., the complex remaining within a highly restricted area and then moving suddenly. This indicates that the movement was promoted by a motive power and constrained by both the 3D structure and protein-protein interactions. The motive power of the movements was produced by blood circulation (essential in processes 1 and 2), diffusion force driven by thermal energy (2, 3 and 4) and active transport by motor proteins (5). The cessation of movement is most likely induced by a structural barricade such as a matrix cage (2, 3, and 4) and/or specific interaction between proteins, e.g., an antibody and HER2 (4), motor proteins, and rail filaments such as actin filaments and microtubules (5).

The molecular mechanism underlying the movement and its cessation during delivery of nanoparticles in animal models is the fundamental basis of drug delivery. There have been many different approaches to tumor-targeting "nanocarriers" including anti-cancer drugs, for passive targeting such as Myocet [18], Doxil [19] and for active targeting such as MCC-465 [20], anti-HER2 immunoliposome [21]. There

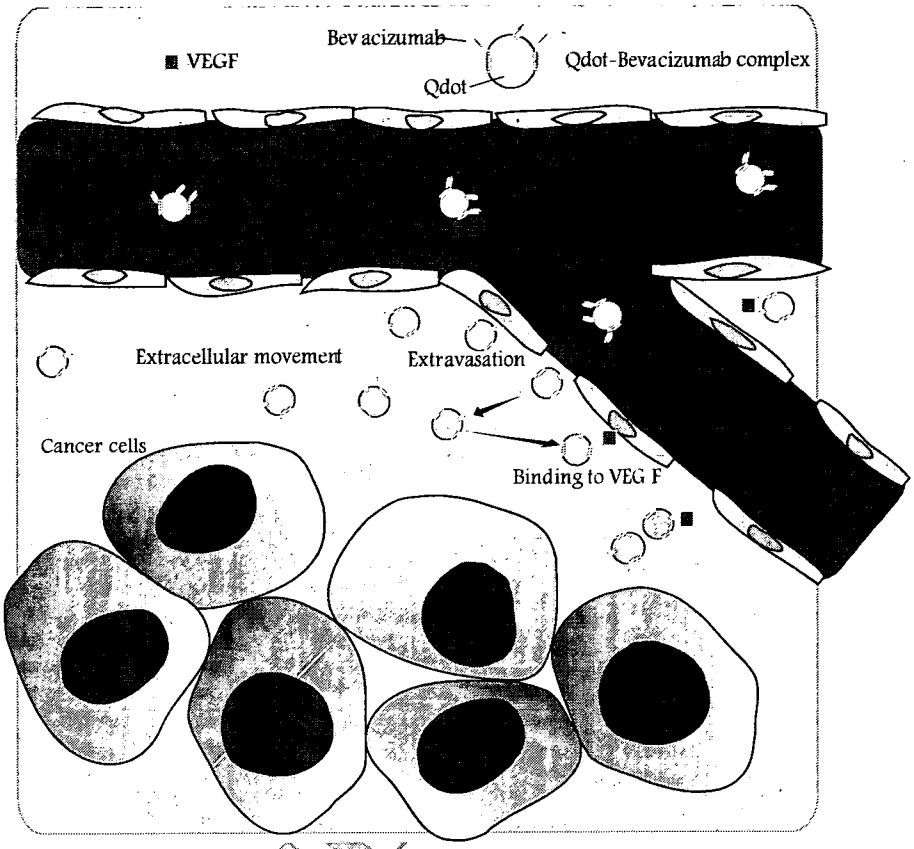

Fig. 4 Delivery of the quantum dots labeled monoclonal antibody. The QT complex in the circulation moved vessel to the interstitial space then bound to the tumor cells. The QT complex finally reached at the nuclear region through intracellular rail protein

is still very little understanding of the biological behavior of nanocarriers, including such crucial features as their transport in the blood circulation, cellular recognition, translocation into the cytoplasm, and final fate in the target cell. These results suggest that the transport of nanocarriers would be quantitatively analyzable in the tumors of living animals by the present method. This approach thus should afford great potential new insight into particle behavior in complex biological environments. Such new insight in turn will allow rational improvements in particle design to increase the therapeutic index of the tumor targeting nanocarriers.

Nanocrystal semiconductor quantum dots conjugated with antibody may serve fundamentally as new controllable materials for medical purposes including cancer molecular imaging.

Homogeneous nanosized beads have shown an advantage for efficient SN detection compared to existing colloids agents of heterogeneous size in the fluorescent nanoparticle study for sentinel navigation surgery. Although the appropriate size for SN detection for human beings is predicted to be 500 nm, and the optimum size may be different between animal species, the appropriate size should be determined for humans with accurately measured nanosized beads of strictly same dimensions.

There are two forms of transportation mechanism regarding a particle material to lymphatic system that is injected into tissue space. One is physical and active extracellular transportation; a particle passes through lymph capillaries. The other one is intracellular transportation of a particle. Foreign materials shift to the lymph capillaries after phagocytosis of particle. An investigation of in vivo dynamics of tracers is important in SN biopsy. It is reported that lymph node was detected by protected graft copolymer combined with Cy5.5, or methoxypolyethyleneglycol-poly-L-lysine combined with Cy5.5 as a tracer. The nanoparticle may distribute to reticuloendothelial system as described in previous reports [22, 23], or may be excreted from kidney for their hydrophilia. We histologically observed liver and kidney 2 weeks after subcutaneous injection of fluorescent beads. Consequently, we did not find beads trapped in liver or kidney by fluorescent microscopic observation, suggesting that the safety of these beads would be ensured when they are given in vivo.

The fluorescent beads that we used are mainly consisted of polystyrene. As polystyrene is the material often used for surgical strings in operation, it would be safe to gave fluorescent beads to living organisms. Accumulation and toxicity are under investigation.

The depth of targets is a serious problem in fluorescence measurement of living tissue. The local excitation illumination within tissue exponentially attenuates due to absorption and scattering from the surface to that depth. This problem of lack of transmission prevents us from detection in tissues deeper than 1 cm from the surface of the body at present [10]. We can detect the SN of small animals like rats, but may have difficulty in detection in larger animals because of the depth at which SNs. For example, lymph node in human is buried in fat and is located deeper than 1 cm. The detection technique to find SN up to 2 cm in depth is recommended. To solve this problem, we should select the appropriate wavelength of fluorescence and fluorescent materials, and also develop imaging techniques. Hemoglobin absorbs light in the range of visible light below 650 nm, and water absorbs light above 1,100 nm, but in the near-infrared range, between 650 and 1,100 nm, the absorption of light in living tissue is minimum. This range is called the optical window. In addition to collagen, NADH and FAD are substances that in vivo have the fluorescent wavelengths in the range of 400–500 nm. So, from this point of view, NIR range has the advantage for the fluorescence measurement. We are also investigating the application of semiconductor nanocrystal that has extremely stronger fluorescent intensity than usual fluorescent beads to increase the detection ability and fluorescence tomography based on acousto-optic modulation imaging [24].

Nanotechnology should be a great aid in improving tailor-made medicine by their hyper-sensitive and super-selective property for diagnoses. Advanced sensing technologies such as the single-molecule imaging technique and acousto-optic modulation imaging technique are also required to make the best use of the functional nanomaterials for achievement of hyper-sensitive and super-selective imaging. These novel products of advanced technologies may realize a revolution of medicine in near future.

This work was supported by Grants-in-aid for Research Projects, Promotion of Advanced Medical Technology (H14-Nano-010 and H18-Nano-001), from the Ministry of Health, Labor and Welfare, Japan.

References

1. Torchilin VP, Lukyanov AN, Gao Z, Papahadjopoulos-Sternberg B. Immunomicelles: targeted pharmaceutical carriers for poorly soluble drugs. Proc Natl Acad Sci USA. 2003;100:6039–44.
2. Krauss WC, Park JW, Kirpotin DB, Hong K, Benz CC. Emerging antibody-based HER2 (ErbB-2/neu) therapeutics. Breast Dis. 2000;11:113–24.
3. Lyons SK. Advances in imaging mouse tumour models in vivo. J Pathol. 2005;205:194–205.
4. Ishijima A, Kojima H, Funatsu T, Tokunaga M, Higuchi H, Tanaka H. Simultaneous observation of individual ATPase, mechanical events by a single myosin molecule during interaction with actin. Cell. 1998;92:161–71.
5. Wu X, Liu H, Liu J, Haley KN, Treadway JA, Larson JP. Immunofluorescent labeling of cancer marker Her2, other cellular targets with semiconductor quantum dots. Nat Biotechnol. 2003;21:41–6.
6. Gao X, Cui Y, Levenson RM, Chung LW, Nie S. In vivo cancer targeting, imaging with semiconductor quantum dots. Nat Biotechnol. 2004;22:969–76.
7. Yildiz A, Forkey JN, McKinney SA, Ha T, Goldman YE, Selvin PR. Myosin V walks hand-over-hand: single fluorophore imaging with 1.5-nm localization. Science. 2003;300:2061–5.
8. Dahan M, Levi S, Luccardini C, Rostaing P, Riveau B, Triller A. Diffusion dynamics of glycine receptors revealed by single-quantum dot tracking. Science. 2003;302:442–5.
9. Lidke DS, Nagy P, Heintzmann R, Arndt-Jovin DJ, Post JN, Grecco HE, Jares-Erijman EA, Jovin TM. Quantum dot ligands provide new insights into erbB/HER receptor-mediated signal transduction. Nat Biotechnol. 2004;22:198–203.
10. Krag DN, Weaver DL, Alex JC. Surgical resection and radiolocalization of the sentinel node in breast cancer using a gamma probe. Surg Oncol. 1993;2:335–40.
11. Tafra L, Lannin DR, Swanson MS. Multicenter trial of sentinel node biopsy for breast cancer using both technetium sulfur colloid and isosulfan blue dye. Ann Surg. 2001;233:51–9.
12. Kurebayashi J, Otsuki T, Tang CK, Kurosumi M, Yamamoto S, Tanaka K, Mochizuki M, Nakamura H, Sonoo H. Isolation and characterization of a new human breast cancer cell line, KPL-4, expressing the Erb B family receptors and interleukin-6. Br J Cancer. 1999;79:707–17.
13. Leunig M, Yuan F, Menger MD, Boucher Y, Goetz AE, Messmer K, Jain RK. Angiogenesis, microvascular architecture, microhemodynamics, and interstitial fluid pressure during early growth of human adenocarcinoma LS174T in SCID mice. Cancer Res. 1992;52:6553–60.
14. Braun RD, Abbas A, Bukhari SO, Wilson W III. Hemodynamic parameters in blood vessels in choroidal melanoma xenografts and rat choroid. Invest Ophthalmol Vis Sci. 2002;43:3045–52.
15. Carraway CA, Carvajal ME, Carraway KL. Association of the Ras to mitogen-activated protein kinase signal transduction pathway with microfilaments. Evidence for a p185 (neu)-containing cell surface signal transduction particle linking the mitogenic pathway to a membrane-microfilament association site. J Biol Chem. 1999;274:25659–67.
16. Buss F, Arden SD, Lindsay M, Luzio JP, Kendrick-Jones J. Myosin VI isoform localized to clathrin-coated vesicles with a role in clathrin-mediated endocytosis. EMBO J. 2001;20:3676–84.
17. Kamal A, Goldstein LS. Connecting vesicle transport to the cytoskeleton. Curr Opin Cell Biol. 2000;12:503–8.
18. Mross K, Niemann B, Massing U, Drevs J, Unger C, Bhamra R, Swenson CE. Pharmacokinetics of liposomal doxorubicin (TLC-D99; Myocet) in patients with solid tumors: an open-label, single-dose study. Cancer Chemother Pharmacol. 2004;54:514–24.
19. O'Brien ME, Wigler N, Inbar M, Rosso R, Grischke E, Santoro A. Reduced cardiotoxicity and comparable efficacy in a phase III trial of pegylated liposomal doxorubicin HCl (CAELYX/Doxil) versus conventional doxorubicin for first-line treatment of metastatic breast cancer. Ann Oncol. 2004;15:440–9.
20. Hamaguchi T, Matsumura Y, Nakanishi Y, Muro K, Yamada Y, Shimada Y. Antitumor effect of MCC-465, pegylated liposomal doxorubicin tagged with newly developed monoclonal antibody GAH, in colorectal cancer xenografts. Cancer Sci. 2004;95:608–13.
21. Park JW, Kirpotin DB, Hong K, Shalaby R, Shao Y, Nielsen UB. Tumor targeting using anti-her2 immunoliposomes. J Control Release. 2001;74:95–113.

22. Josephson L, Mahmood U, Wunderbaldinger P, Tang Y, Weissleder R. Pan and sentinel lymph node visualization using a near-infrared fluorescent probe. Mol Imaging. 2003;2:18–23.
23. Patrick W, Karl T, Chrstoph B. Near-infrared fluorescence imaging of lymph nodes using a new enzyme sensing activatable macromolecular optical probe. Eur Radiol. 2003;13:2206–11.
24. Kobayashi M, Mizumoto T, Shibuya Y, Takeda M, Enomoto M. Fluorescence tomography in turbid media based on acousto-optic modulation imaging. Appl Phys Lett. 2006;89:1811022

1-6 機能性ナノ粒子による生体イメージング —がん診療への応用—

武田元博 東北大学大学院医学系研究科
小林芳男 茨城大学工学部生体分子機能工学科
小林正樹 東北工業大学知能エレクトロニクス学科
桜井 遊 東北大学大学院医学系研究科
甘利正和 東北大学大学院医学系研究科
石田孝宣 東北大学大学院医学系研究科
鈴木昭彦 東北大学大学院医学系研究科
大内憲明 東北大学大学院医学系研究科

1 はじめに

ナノテクノロジーにおける物質創製は，分子レベルで物質を合成するボトムアップ法と，従来存在する物質の分解・分割で小さな物質を新たに創り出すトップダウン法の，2つの異なる物質制御技術からなる．さらに近年in-silico designと呼ばれる，シミュレーションによって有用・安定な化学構造を予測し合成する手法や，合成した物質の物性から構造を予測する手法が出現するなど，多くの工学分野がナノテクノロジーに関与している．

これらナノレベルの物質制御技術は，現在急速な勢いで発展し，そこから生み出されたさまざまな物質は，われわれの生活を大きく変える可能性を秘めている．たとえば，ナノサイズへ微小化された電子回路の部品や，これらを組み合わせてできたデバイスによるマイクロまたはナノサイズの装置や，新たな機能を付与して創製された分子・クラスターなどの物質が挙げられ，これらの技術は従来の“もの作り”をベースとして，シミュレーションやナノメートルオーダーの計測技術などの新しい技術を巻き込みながらさらに発展していこうとしている．

このように，ナノテクノロジーは従来にはない機能を持った物質を生み出しつつあり，それらは医療においても利用可能と考えられることから，現在，その応用が試み始められている．さまざまな疾患の中で，がんは1985年以降，日本人の死因の第1位を占めており，働き盛りの年代のがん死は人口の急速な高齢化が進むわが国において，もっとも緊急に改善しなければならない課題の